Unified Deep Learning Framework for Many-Body Quantum Chemistry via Green's Functions

Christian Venturella, Jiachen Li, Christopher Hillenbrand, Ximena Leyva Peralta, Jessica Liu, and Tianyu Zhu [*]

Department of Chemistry, Yale University, New Haven, CT, USA 06520

Abstract

Quantum many-body methods provide a systematic route to computing electronic properties of molecules and materials, but high computational costs restrict their use in large-scale applications. Due to the complexity in many-electron wavefunctions, machine learning models capable of capturing fundamental many-body physics remain limited. Here, we present a deep learning framework targeting the many-body Green's function, which unifies predictions of electronic properties in ground and excited states, while offering deep physical insights into electron correlation effects. By learning the *GW* or coupled-cluster self-energy from mean-field features, our graph neural network achieves competitive performance in predicting one- and two-particle excitations and quantities derivable from one-particle density matrix. We demonstrate its high data efficiency and good transferability across chemical species, system sizes, molecular conformations, and correlation strengths in bond breaking, through multiple molecular and nanomaterial benchmarks. This work opens up new opportunities for utilizing machine learning to solve many-electron problems.

---

[*]tianyu.zhu@yale.edu

Introduction

Predicting electronic properties of molecules and materials in ground and excited states is a central task in quantum chemistry and computational materials science. Density functional theory (DFT) has been the primary tool for this task due to balanced accuracy and efficiency [1], but it has well-known systematic errors and uncertainties stemming from approximate exchange-correlation functionals [2], which limit its predictive capability. Ab initio many-body electronic structure methods, such as coupled-cluster (CC) theory [3] and many-body perturbation theory (*GW*) [4, 5], offer a promising route to more robust quantum mechanical simulations. These methods are particularly desired in the simulations of catalysis and materials that require explicit treatment of electron correlation, such as bond-breaking and excited-state phenomena as well as transition metal compounds. However, their high computational costs prohibit their application to the study of large systems or screening of many molecules.

Data-driven machine learning (ML) has been extensively explored to accelerate quantum chemistry calculations at different levels of theory [6–14]. These ML models mostly focus on predicting the potential energy or one electronic property (e.g., dipole moment, orbital energy) at a time. Recently, ML models aiming at more fundamental quantum mechanical quantities, such as the mean-field Hamiltonian [15, 16], electron density [17–19], and one-particle density matrix [20], start to appear, where various electronic properties can be derived following a single ML prediction. Nevertheless, these methods are usually developed for DFT and limited by its inherent errors, while ML approaches capable of predicting both ground- and excited-state many-body properties within a unified framework remain rare. The main reason is that the size of many-electron wavefunction grows rapidly (at least with high polynomial scaling) with respect to the molecular size, resulting in patterns that are too complex to learn. Electron density (or density matrix) computed at the many-body level could serve as the ML target, but directly mapping ground-state electron density information to excited states is a non-trivial task [21]. Furthermore, generating many-body quantum chemistry training data is very expensive, which requires the ML method to be highly data-efficient.

In this work, we propose to use the many-body Green's function (MBGF) as the central quantity to enable a deep learning framework that seamlessly connects ground- and excited-state predictions at quantum many-body level. The Green's function $G(\omega)$ is a frequency-dependent quantity that describes the propagation

of an electron/hole in a many-electron system. The size of MBGF grows quadratically with respect to the system size, making it a more compact representation of many-body physics compared to the wavefunction. The Green's function theory provides a rigorous road map towards solving the Schrödinger equation exactly by simulating the one-particle (charged) and two-particle (neutral) excitations through Hedin's equation and Bethe-Salpeter equation (BSE) [22, 23]. In addition to excited states, MBGF also contains most of the essential ground-state information. Its static limit yields the one-particle density matrix, while integrating MBGF along the imaginary frequency axis gives the ground-state energy. In recent years, ab initio MBGF methods have achieved great success for simulating correlated molecules and materials, based on *GW* [4, 5, 24, 25], CC [26–29], second-order perturbation theory [30, 31], algebraic diagrammatic construction [32], density matrix renormalization group [33], and quantum Monte Carlo [34]. MBGF is also the central quantity in quantum embedding methods including dynamical mean-field theory [35–37] and self-energy embedding theory [38]. Thus, an MBGF-based ML approach will not only unify predictions of many electronic properties of interest, but also offer fundamental insights into electron correlation effects across a large number of molecular and material problems.

A major challenge in developing this ML method is to represent the frequency-dependent MBGF matrix of a molecule in a compact and equivariant form, while capturing both local and non-local electron correlations encoded in MBGF. We achieve this by developing a graph neural network (GNN) that directly learns the many-body dynamical correlation potential (i.e., self-energy) on a compact imaginary frequency grid, using orbital-based mean-field features in a symmetry- and polarization-adapted basis. This method raises our recent work [39] to a new level, offering substantially better capability and accuracy than related works [40, 41], and we name the resulting model MBGF-Net. On a series of molecular and nanomaterial benchmark problems, we show that MBGF-Net accurately predicts ground- and excited-state properties, including photoemission and optical spectra, quasiparticle energies and renormalizations, as well as quantities derivable from one-particle density matrix, at the levels of *GW* and coupled-cluster singles and doubles (CCSD). We find that MBGF-Net is highly data-efficient, predicting *GW* frontier quasiparticle energies of QM7/QM9 molecules with mean absolute errors under 0.02 eV using a training set of only 2,000 molecules. Furthermore, we demonstrate promising transferability of MBGF-Net across different chemical species, molecular conformations, system sizes, and electron correlation strengths. In particular, the MBGF-Net model trained

exclusively on small silicon nanoclusters predicts excitation spectra of silicon nanoclusters up to four times larger with minimal loss of accuracy. The MBGF-Net approach thus provides a unified framework for ML-accelerated many-body quantum chemistry simulations, opening up new opportunities for data-driven ML in the underexplored regimes of correlated electron problems.

Results

MBGF graph neural network. While geometric deep learning has been widely used in chemical applications [14, 42, 43], the MBGF is a unique ML target that requires careful attention to molecule featurization and GNN architecture. The Green's function matrix in the frequency domain is defined as

$$G_{ij}(\omega) = \left\langle \Psi_0 \,\middle|\, a_i[\omega - (\hat{H} - E)]^{-1}a_j^\dagger \,\middle|\, \Psi_0 \right\rangle + \left\langle \Psi_0 \,\middle|\, a_j^\dagger[\omega + (\hat{H} - E)]^{-1}a_i \,\middle|\, \Psi_0 \right\rangle \quad (1)$$

where ω is the frequency (energy), $|\Psi_0\rangle$ is the ground-state wave function, $\hat{H}$ is the Hamiltonian, E is the ground-state energy, and a_i and $a_j^\dagger$ are annihilation and creation operators on orbitals i and j. Our goal is to design an orbital-based graph neural network that predicts the MBGF matrix in a given basis set from DFT or Hartree-Fock (HF) solution, thereby bypassing the expensive many-body quantum chemistry calculation. Similar to many ab initio MBGF theories, instead of directly computing $G(\omega)$, MBGF-Net predicts the self-energy, defined through the Dyson's equation

$$\Sigma(\omega) = G_0^{-1}(\omega) - G^{-1}(\omega). \quad (2)$$

Here, the self-energy $\Sigma(\omega)$ captures dynamical (i.e., energy-dependent) many-body correlation effects missed by the mean-field Green's function $G_0(\omega)$. Thus, the self-energy $\Sigma(\omega)$ is a natural physics-informed Δ-ML target, as $G_0(\omega)$ is always pre-calculated in our workflow.

As shown in Fig. 1a, we adopt an intrinsic atomic orbital plus projected atomic orbital (IAO+PAO) basis [44] widely used in population analysis and quantum embedding methods to represent all matrices, where the atomic orbitals are polarized by the molecular environment. To ensure rotation invariance, we further apply an angular-momentum block diagonalization step to obtain symmetry-adapted IAO+PAO basis [14, 39],
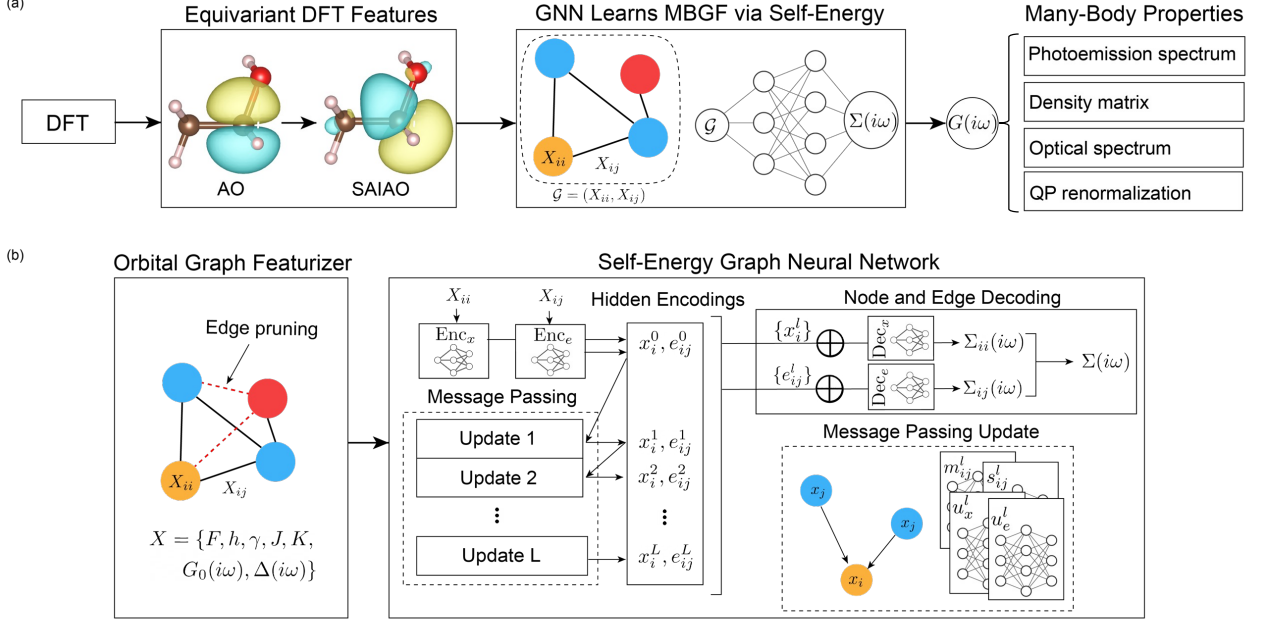
Figure 1: Overview of the MBGF-Net workflow and architecture. (a) Starting from a DFT calculation, equivariant DFT features are constructed in the SAIAO basis and mapped onto the orbital graph. After self-energy and MBGF are predicted, MBGF is post-processed to obtain various ground- and excited-state properties at quantum many-body level. (b) The orbital graph is constructed by mapping diagonal and off-diagonal DFT matrix elements to nodes and edges. Edges are pruned based on an orbital interaction criterion. Node and edge features are then autoencoded with corresponding residual blocks. These first hidden encodings are passed to L message passing updates. All $L + 1$ hidden node and edge encodings are vector-concatenated ($\bigoplus$) and finally decoded into diagonal and off-diagonal self-energy.

which we refer to as the SAIAO basis. To deal with the continuous frequency dependence in dynamical quantities, we express $\Sigma(i\omega)$ and $G(i\omega)$ on a modified Gauss-Legendre grid along the imaginary frequency axis ($N_\omega = 18 \sim 30$). This choice leads to much smoother self-energy and MBGF for ML, which also allows straightforward post-processing of ML-predicted $G(i\omega)$ to access ground-state and spectral properties. Specifically, by analytically continuing $G(i\omega)$ to the real-axis $G(\omega)$, one obtains the photoemission spectrum (i.e., density of states, DOS) with a broadening factor η

$$\text{DOS}(\omega) = -\frac{1}{\pi}\text{Tr}\left[\text{Im}G(\omega + i\eta)\right]. \tag{3}$$

Within the *GW* approximation, the optical spectrum can be further computed at a reduced cost by utilizing the ML-predicted quasiparticle (QP) energies via the *GW*+BSE formalism [23]. The one-particle reduced

density matrix (1-RDM) is obtained through efficient numerical integration

$$\gamma = \frac{1}{\pi} \int_0^\infty G(i\omega)d\omega. \tag{4}$$

In addition, the self-energy curvature encodes orbital-specific electron correlation strength, indicated by the magnitude of the quasiparticle renormalization (a value between 0 and 1)

$$Z_i = \left[1 - \frac{\partial \left[\text{Im}\Sigma_{ii}(i\omega) \right]}{\partial \omega} \bigg|_{\omega=0} \right]^{-1}, \tag{5}$$

where smaller value of Z_i corresponds to stronger electron correlation in orbital i.

In MBGF-Net, we take inspirations from OrbNet [14, 45] to employ DFT (or HF) electronic matrices as features, while predicting frequency-dependent self-energy vectors for every orbital and orbital pair $\Sigma_{ij}(i\omega)$ (instead of molecular scalar quantities). As shown in Fig. 1b, diagonal and off-diagonal DFT matrix elements are respectively mapped onto the nodes and edges of the orbital graph. In addition to static features including Fock (F), core Hamiltonian (h), Coloumb (J), exchange (K), and density (γ) matrices, a new set of dynamical features (mean-field Green's function $G_0(i\omega)$ and hybridization function $\Delta(i\omega)$) inspired by ab initio MBGF theories [5, 35–37] is also employed, which was found to be more effective for MBGF prediction previously [39]. To reduce the number of edges (N_{orb}^2 with N_{orb} being the number of orbitals) in these graphs, we prune edges when $\max(|J_{ij}|, |K_{ij}|) < \epsilon$ between an orbital pair i and j, where ϵ is a small cutoff value. This criterion supposes that two orbitals with negligible bare interaction also have negligible many-body correlation, an assumption similar to integral screening metrics used in low-scaling *GW* techniques [46]. For edges removed from the orbital graph, the orbital-pair self-energy is set to zero.

The MBGF-Net architecture is presented in Fig. 1b, with further technical details provided in the Methods section and the Supplementary Information (SI). We use an encoder-decoder scheme to learn self-energy frequency responses over the nodes and edges of the orbital graph. For message passing between orbitals i and j, the following transformation of their node features x ensures pair permutation invariance without loss of degrees of freedom:

$$\tilde{x}_i = x_i + x_j, \ \ \tilde{x}_j = |x_i - x_j|. \tag{6}$$

$\tilde{x}_i$ and $\tilde{x}_j$ are then utilized in message functions m^l and attention score functions s^l. Then, single-headed attentional aggregation is employed for each message passing update l, followed by single layer node update u_x^l and edge update u_e^l:

$$x_i^{l+1} = u_x^l \left(\sum_{j \in \mathcal{N}(i)} \frac{\exp(s_{ij}^l) m_{ij}^l}{\sum_{j \in \mathcal{N}(i)} \exp(s_{ij}^l)} \right), \ \ e_{ij}^{l+1} = u_e^l(m_{ij}^l). \tag{7}$$

Tuning of the architecture is mostly done via two key parameters: the number of channels in the message passing layers N_c (i.e. the width of each hidden encoding) and the number of message passing updates L. N_c can be increased to enhance model capacity to accommodate a more diverse chemical space, while L can be increased to express a higher degree of orbital entanglement for stronger correlation or more spatially delocalized electronic structure.

Many-body quantum chemical properties in ground and excited states.   We first benchmark the performance of MBGF-Net for predicting various quantum many-body properties in ground and charged excited states on a data set consisting of all QM7 molecules (7,165) [47] and a subset of QM9 molecules (8,000) [48]. We generated the training data at the G_0W_0@PBE0 level in the cc-pVDZ basis set [49, 50] with the PySCF quantum chemistry software package [24, 51], using at most 2,000 molecules for training and reserving the remaining 13,165 molecules for testing. We also augmented the training data with 20 conformers for each molecule that contains 3 or fewer heavy atoms (660 conformers).

Fig. 2 summarizes the MBGF-Net results, where the baseline DFT calculation used the PBE0 functional [52] and all quantities were derived from the MBGF-Net model trained exclusively on the self-energy data. In Fig. 2a, five MBGF-Net ensemble models were trained on successively larger training sets. The first subset consisted of the smallest 395 molecules with 5 or fewer heavy atoms, while larger molecules (7 or 9 heavy atoms) were randomly added in the training of subsequent models. We employed a physics-motivated loss function that imposes additional penalties on the self-energy errors on frontier molecular orbitals (FMO) and frequency gradients

$$\mathcal{L} = \mathcal{L}_{\mathrm{MSE}}(\hat{\Sigma}^{\mathrm{SAIAO}}, \Sigma^{\mathrm{SAIAO}}) + \beta_1 \mathcal{L}_{\mathrm{MSE}}(\hat{\Sigma}_{ii}^{\mathrm{MO}}, \Sigma_{ii}^{\mathrm{MO}}; i \in \mathrm{FMO}) + \beta_2 \mathcal{L}_{\mathrm{MSE}}(\frac{\partial \hat{\Sigma}^{\mathrm{SAIAO}}}{\partial \omega}, \frac{\partial \Sigma^{\mathrm{SAIAO}}}{\partial \omega}) \tag{8}$$
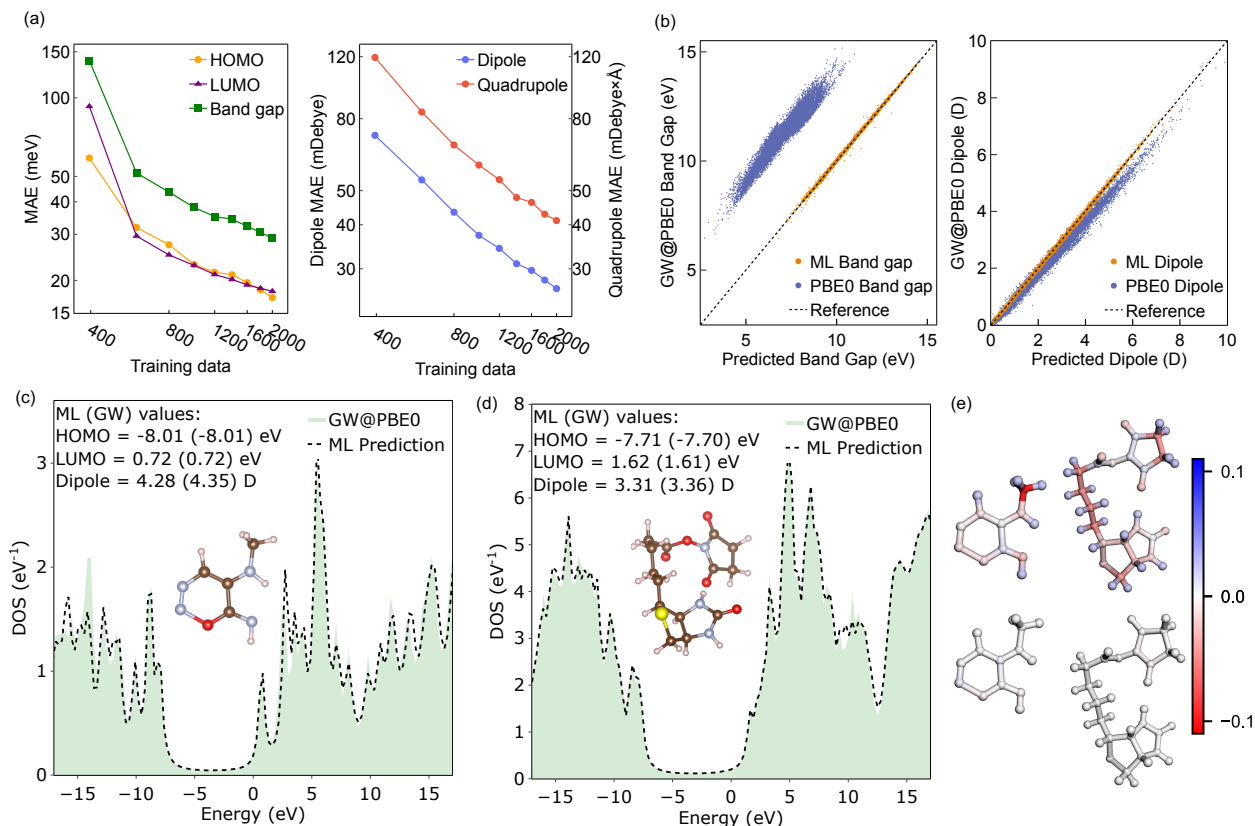
Figure 2: MBGF-Net predictions of electronic properties of QM7 and QM9 molecules at the G_0W_0@PBE0 level. (a) Training curves for HOMO, LUMO, band gap, and dipole and quadrupole moments from a single ML model trained using only the self-energy data. MAE stands for mean absolute error. (b) Scatter plots comparing ML-predicted band gaps and dipole moments against PBE0 (baseline) and true G_0W_0@PBE0 values. (c) Prediction of DOS, HOMO, LUMO, and dipole moment on an interpolation case ($C_4H_6N_4O$). True G_0W_0@PBE0 values are included in the parentheses for comparison. (d) Prediction of same quantities as (c), but on an extrapolation case of NHS-biotin ($C_{14}H_{19}N_3O_5S$). (e) Comparison of IAO atomic partial charge errors of DFT (top) and ML (bottom) for interpolation and extrapolation cases. Partial charge errors are indicated by the blue or red color.

where $\hat{\Sigma}$ and Σ denote ML-predicted and true self-energy values in SAIAO or molecular orbital (MO) basis, MSE denotes mean-squared error, and β_1 and β_2 control the relative weights of the extra penalty terms. Unless otherwise stated, we set $\beta_1 = \beta_2 = 0.1$. Additional results adopting an active learning strategy can be found in the SI.

In Fig. 2a, we find that the mean absolute errors (MAEs) of all ML-predicted quantities drop quickly as more molecules are added into the training set. For the model trained on 2,000 molecules, the MAEs of HOMO

(highest occupied molecular orbital) and LUMO (lowest unoccupied molecular orbital) QP energies and band gaps are only 17, 18, and 29 meV, respectively. This performance surpasses that of some state-of-the-art deep learning models (e.g., DimeNet++ and SchNet) on a similar task [53]. For example, DimeNet++ has larger MAEs for predicting G_0W_0 HOMO, LUMO, and band gap energies (22, 31, 42 meV) on the QM9 data set starting from DFT calculations, even with 10^5 molecules in the training set ($50\times$ larger than current work) [53]. From the same model, the 1-RDM predicted by MBGF-Net is of similarly high quality, indicated by small dipole and quadrupole moment MAEs of 26 mD and 41 mD·Å. The error distributions are shown in Fig. 2b, where ML-predicted band gaps and dipole moments are compared against the baseline PBE0 and true G_0W_0@PBE0 values. We then present two case studies in Fig. 2c,d: a QM9 molecule ($C_4H_6N_4O$), considered an interpolation task, and a larger molecule, NHS-biotin ($C_{14}H_{19}N_3O_5S$), considered an extrapolation task. We note that the size of NHS-biotin is more than twice larger than any molecule in the training set. ML-predicted photoemission spectra are in excellent agreement with the G_0W_0@PBE0 spectra for both molecules over a wide energy range. Atomic partial charges derived from the ML-predicted MBGFs also agree perfectly with the true G_0W_0@PBE0 values in both cases (Fig. 2e). Overall, this benchmark demonstrates that MBGF-Net, by learning the many-body electron correlation effects through the self-energy, achieves accurate predictions of many electronic properties with high data efficiency and can generalize to larger molecules well outside the training set.

Transferability across nanomaterials and molecular systems. We then demonstrate the transferability of MBGF-Net in more challenging photophysics applications. In particular, we aim to push its good capabilities in small organic molecules to achieve many-body simulations of large-scale materials, where traditional theoretical studies are mostly restricted to DFT-based methods. We trained an MBGF-Net model on 160 hydrogenated silicon (Si) nanoclusters with up to 36 Si atoms ($N_{Si} \leq 36$), for predicting photophysical properties of nanoclusters of sizes up to 147 Si atoms. The training and testing data were generated at the G_0W_0@PBE0 level in the cc-pVTZ basis set, on structures taken from Refs. [55, 56] (Fig. 3b). In addition to charged excitations, we also utilized the ML-derived GW QP energies across the full energy range for the downstream task of computing neutral (optical) excitation energies and spectra via the GW+BSE formalism (see SI for details). MBGF-Net allows us to bypass the GW step in the GW+BSE calculation, which is more expensive than the BSE step, thus significantly reducing the computational cost.
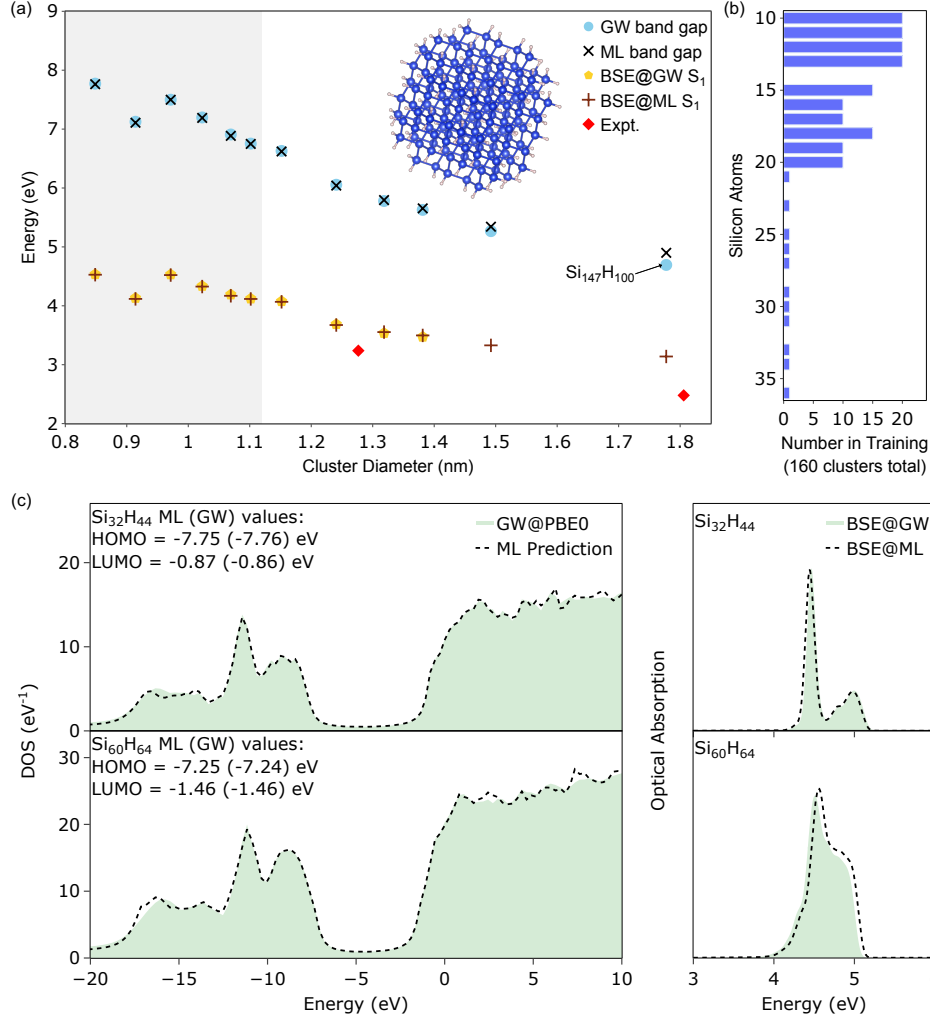
9

Figure 3: MBGF-Net predictions of excited-state properties of silicon nanoclusters at the G_0W_0@PBE0 level. (a) Band gaps and optical gaps (S_1) for silicon clusters of increasing diameters, assuming a density of 50 Si atoms/nm^3 as in bulk silicon. Optical gaps were obtained by solving the BSE equation with true GW or ML-predicted QP energies, denoted as BSE@GW or BSE@ML. Grey shaded region indicates interpolation regime ($N_{\text{Si}} \leq 36$ and not seen in the training), while the largest extrapolation case is $\text{Si}_{147}\text{H}_{100}$ (2158 electrons, 6398 orbitals). Experimental optical gap values are taken from Ref. [54]. (b) Size distribution of training data. (c) Photoemission and optical spectra for $\text{Si}_{32}\text{H}_{44}$ (interpolation) and $\text{Si}_{60}\text{H}_{64}$ (extrapolation). The lowest 60 and 240 singlet excited states were solved in the GW+BSE calculations of $\text{Si}_{32}\text{H}_{44}$ and $\text{Si}_{60}\text{H}_{64}$.

As shown in Fig. 3a, MBGF-Net yields near-perfect predictions of band and optical gaps with errors under 25 and 24 meV, not only for Si nanoclusters in the interpolation regime (i.e., $N_{\text{Si}} \leq 36$ and not seen in the training), but also for clusters up to $\sim 2\times$ larger than any training sample (e.g., $\text{Si}_{69}\text{H}_{68}$). This performance significantly outperforms a recently-proposed ML method in accelerating GW calculations on the same data

10

set [55], which suggests that our GNN design is effective in capturing long-range screening effects. It should be emphasized that only 11 out of 160 training samples have $N_{\text{Si}} > 20$ (Fig. 3b), highlighting the data efficiency of our method. Even for the largest two testing clusters up to $4\times$ larger than any training sample, $\text{Si}_{87}\text{H}_{76}$ and $\text{Si}_{147}\text{H}_{100}$, the band gap errors remain small (75 and 206 meV). Due to the prohibitive cost of computing the full GW QP energy spectra, we were unable to perform true BSE@GW calculations to compare with BSE@ML for these two largest clusters. In Fig. 3c, we show that MBGF-Net also predicts highly accurate photoemission and optical spectra for $\text{Si}_{32}\text{H}_{44}$ and $\text{Si}_{60}\text{H}_{64}$, which contain hundreds of excited states. These results demonstrate impressive transferability of MBGF-Net, which has the potential to enable simulating excited states of large-scale materials beyond the reach of traditional quantum many-body methods.
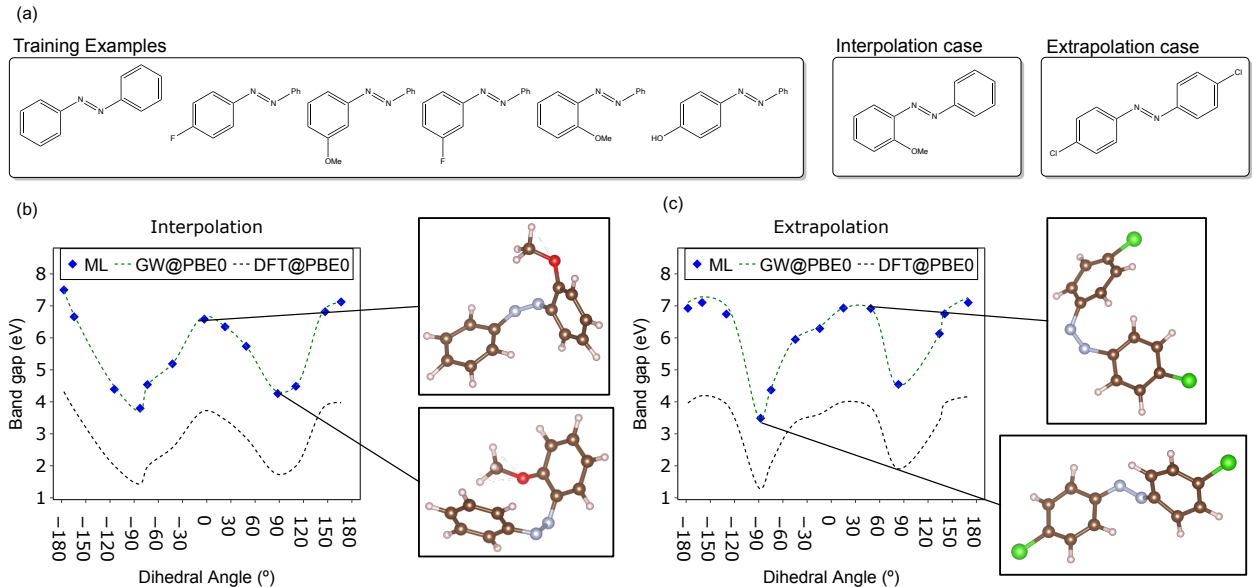

Figure 4: MBGF-Net predictions of band gaps of azobenzene derivatives at the G_0W_0@PBE0 level. (a) Summary of training data and test cases. (b) Prediction of band gaps as the CN=NC dihedral angle varies for 2-methoxyazobenzene (interpolation case), compared against true G_0W_0@PBE0 and DFT-PBE0 values. The energy profiles are splined to ease viewing. (c) Prediction of band gaps as the CN=NC dihedral angle varies for 4,4'-dichloroazobenzene (extrapolation case).

In Fig. 4, we also test whether MBGF-Net can capture subtle electronic structure changes due to conformational distortions, where a model was trained on 100 conformations each of 6 azobenzene derivatives (Fig. 4a), at the G_0W_0@PBE0 level in the cc-pVTZ basis. The full range of the CN=NC dihedral for each

derivative was sampled with ab initio molecular dynamics (AIMD) by applying a small bias potential to this torsion using the CP2K software package [57]. In Fig. 4b, we show that MBGF-Net predicts highly accurate band gaps of 2-methoxyazobenzene conformers with distorted CN=NC dihedral angle, considered an interpolation case (similar 2-methoxyazobenzene conformers seen in training). Beyond this task, we also applied the same model to 4,4'-dichloroazobenzene (Fig. 4c), which is completely unseen in the training data. This extrapolation case falls outside the training data both in terms of atomic composition (chlorine) and substitution pattern (all training examples are singly substituted). ML-predicted band gaps again agree well with true G_0W_0@PBE0 values, suggesting good transferability across conformations and chemical species. To emphasize that MBGF-Net is not simply learning a constant band gap shift, we also provide the energy profiles aligned at minimum band-gap geometry in the SI, which show the relative many-body corrections captured by MBGF-Net to be on the order of 0.5 eV.

Strong electron correlation in bond-breaking molecules. We lastly explore the capability of MBGF-Net in the strong electron correlation regime, where quantum many-body treatment beyond DFT (and even *GW*) must be used for reliable simulations. We target the cases of C-O single-bond breaking in methanol and ethanol, where CCSD is a reasonable compromise between accuracy and efficiency. We trained an MBGF-Net model on 100 methanol geometries sampled along the C-O stretch and 50 ethane molecules sampled along the C-C stretch (bond length range of 1.3~4.0 Å), where the training data were the self-energies computed at the equation-of-motion CCSD level (also known as coupled-cluster Green's function, CCGF) [28, 29] in the cc-pVTZ basis. All training and testing stretched structures were sampled using metadynamics in CP2K. All mean-field features were generated at the HF level and the extra loss penalties in Eq. 8 were removed in training ($\beta_1 = \beta_2 = 0$).

We first show how MBGF-Net uncovers fundamental insights into orbital-specific electron correlation, which cannot be obtained from DFT calculations. QP renormalizations predicted by MBGF-Net are presented in Fig. 5a, a quantity commonly used for indicating strength of electron correlation in many-body physics [35, 58]. We find that MBGF-Net achieves near-perfect agreement for HOMO and LUMO Z values of methanol along the C-O stretch, even in the very strongly correlated regime (indicated by small $Z = 0.2 \sim 0.3$). For extrapolating to the ethanol C-O stretch, MBGF-Net exhibits good, but worsened
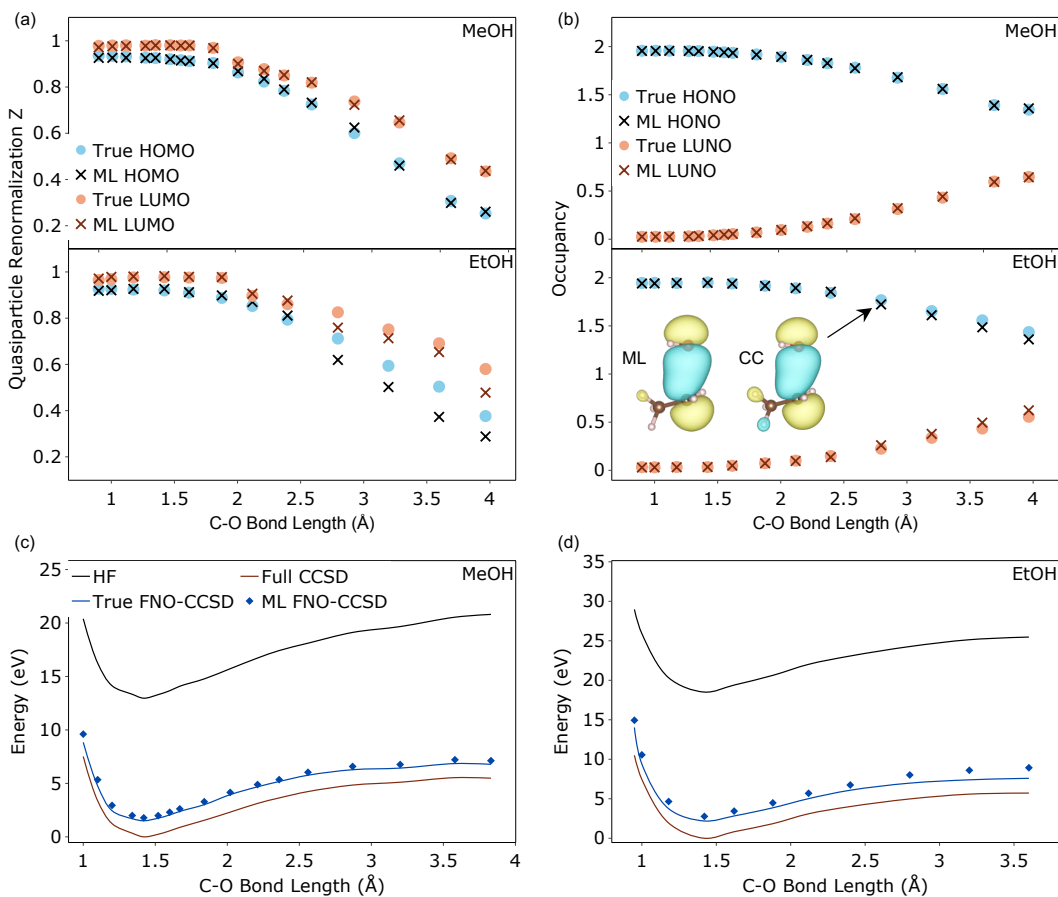
Figure 5: MBGF-Net predictions of orbital-specific many-body properties and downstream simulations in C-O single-bond breaking. Training data includes 100 methanol and 50 ethane molecules. (a) Quasiparticle renormalization weights Z of frontier MOs as the C-O bond length increases in methanol and ethanol. (b) Natural occupancies of HONO (highest occupied natural orbital) and LUNO (lowest unoccupied natural orbital) as the C-O bond length increases in methanol and ethanol. ML and true HONOs are shown for ethanol at C-O bond length of 2.8 Å. (c) Ground-state energies of methanol calculated by FNO-CCSD using ML-predicted virtual natural orbitals (threshold 5×10^{-4}), compared against HF, FNO-CCSD with true CCSD NOs, and full CCSD. The potential energy curves are not perfectly smooth as the geometries are relaxed using metadynamics. All curves are shifted by the equilibrium CCSD energy. (d) Same as (c), but for ethanol.

agreement, with systematic errors towards over-correlated Z for a stretched C-O bond, a result of only seeing methanol and ethane in training. In Fig. 5b, we derive natural orbitals by diagonalizing the correlated 1-RDM predicted by MBGF-Net: $\gamma V = V n$, where V and n are the natural orbitals (NOs) and NO occupancies. The concept of natural orbitals is widely used in quantum chemistry for analyzing chemical bonding and electron correlation as well as accelerating correlated calculations. MBGF-Net yields accurate

13

predictions of NO occupancies for HONO (highest occupied natural orbital) and LUNO (lowest unoccupied natural orbital) of both methanol and ethanol, where the extent of deviation from integer fillings (0 and 2) indicates the correlation strength along the C-O stretch.

We note that, although it is possible to obtain ground-state energy directly from the integration of MBGF, we leave it to future work due to the numerical sensitivity of this integration to MBGF errors. Instead, we employ ML-predicted CCSD natural orbitals in the downstream task of computing ground-state energies using the frozen natural orbital CCSD (FNO-CCSD) approach [59]. By freezing the virtual natural orbitals with natural occupancies smaller than a given threshold (5×10^{-4} in this work), FNO-CCSD captures a large fraction of CCSD correlation energy at a reduced cost compared to full CCSD, as shown in Fig. 5c,d. In this study, the FNO-CCSD virtual space is only 1/3 of the full virtual space for methanol and ethanol, corresponding to $\sim$81-fold reduction of computational cost. We find that FNO-CCSD energies based on ML-predicted NOs agree well with those based on true CCSD NOs in the case of methanol. The agreement deteriorates slightly for ethanol, especially in the most strongly correlated regime (long bond lengths). Nevertheless, in both cases, ML FNO-CCSD predictions are significantly better than HF and have small non-parallelity errors compared to full CCSD (errors in energy differences between equilibrium and stretched geometries, see SI). In summary, this benchmark demonstrates that MBGF-Net can serve as a unified quantum many-body tool for studying correlated electron systems with deep physical insights.

Discussion

We have developed a deep learning method for predicting quantum many-body properties of molecules and materials from the DFT electronic structure. Unlike many other approaches, we undertake the challenging task of directly learning the underlying many-body effects with a single ML model, that can be leveraged to predict various ground- and excited-state properties at once. We have demonstrated that MBGF-Net achieves near-perfect accuracy on systems similar to the training data, while being transferable to systems well outside the training data, both in terms of size and composition. Our method is also data efficient, needing only hundreds of training molecules in most benchmarks, which ameliorates the high costs of generating many-body quantum chemistry data. Because of its direct targeting of the Green's function and

self-energy, MBGF-Net can analyze the physical origins of many-body electron correlation effects in many-electron systems, a capability rarely seen in other data-driven ML models. Even in challenging extrapolation cases that expose limitations of our method, we argue that useful insights into the nature of electronic interactions can still be drawn. For example, the overestimation of band gaps in Si nanoclusters (e.g., $Si_{147}H_{100}$) much larger than training samples suggests the long-range nature and length scale of screened Coulomb interactions. Moreover, MBGF-Net can be seamlessly integrated into widely-used ab initio MBGF frameworks, e.g., as data-driven impurity solvers within Green's function embedding methods [36, 37, 60], for simulating correlated electron materials. Overall, this work establishes a unified ML framework for many-body quantum chemistry and demonstrates the possibility of ML-accelerated computational study of many-electron systems towards quantitative accuracy.

Methods

GNN architecture. As shown in Fig. 1b, two residual networks each encode the nodes and edges. Because we suppose the static, dynamical, and binary features carry different types of information, they are initially passed to three independent linear layers before concatenation in the deeper portion of the residual networks. Two independent decoders are used for node and edge self-energy, though the architecture for each is identical. Detailed descriptions for the encoders, message function, attention score function, and decoders can be found in the SI, in addition to MBGF-Net hyperparameters for each learning task. The core data processing and architecture for our GNN are implemented with the PyTorch and Pytorch Geometric libraries [61, 62], with the attentional aggregation implementation from previous works [63, 64].

Orbital feature processing and graph construction. In addition to the static and dynamic features we used in our previous work, we utilize the spatial extent of each orbital and IAO atomic partial charges on the atom associated with a given orbital. We employ these only on the nodes and consider them static due to lack of any frequency dependence. For node features, we take care to account for the potentially large magnitudes of h_{ii} and J_{ii}. These elements cancel each other out, so we use their sum as the feature to avoid numerical problems when unseen (larger than training) systems are passed to MBGF-Net. In addition to continuous valued features, we also utilize simple binary (i.e., one-hot) features on the nodes, corresponding to orbital

15

type (core/IAO/PAO), principal number (n), and angular momentum number (ℓ). All continuous valued features on nodes are transformed to have unit variance and zero mean (i.e., standardized). Edge features are processed with a log transformation detailed in the SI.

The self-energy elements associated with core orbitals are set to zero. During the SAIAO construction step for the Si nanocluster and bond breaking benchmarks, the core orbitals are projected separately, to avoid mixing the SAIAO core orbitals with the valence and virtual orbitals.

Self-energy loss. In Eq. 8, aside from changing values of β_i, tuning for specific applications is mostly done via the definition of the FMOs. If the set of FMOs is too small (e.g., fitting to only the HOMO/LUMO self-energy), we observe the training loss oscillates unfavorably in the later part of the optimization. For the QM9 molecules, we find including the range of HOMO $-$ 10 to LUMO $+$ 10 is reasonable, but fixing this range to a constant number is problematic for datasets with highly variable system sizes. For example, with silicon nanoclusters, we instead employ a scheme where percentages of occupied/virtual are included into the set of FMOs. We forego any parameter search and select 30%/25% for occupied/virtual MOs to capture all valence occupied orbitals and virtual orbitals up to approximately 20 eV.

Active learning strategies. We explore the effectiveness of active learning approaches for learning MBGF for the QM7/QM9 learning task to deal with the high diversity of chemical compositions. In particular, we observe that this dataset has relatively few molecules with functional groups of potential interest to photophysical applications – for example, QM7/QM9 have very few sulfur/fluorine containing compounds. This suggests that a naively trained MBGF-Net may have a bias that reflects the inherent imbalance of the underlying data. To address this, we implement a training strategy we call "active refinement" that optimizes a pre-trained ensemble model with a focus on the most unusual training examples - the detailed algorithm can be found in the SI. For Fig. 2, we employ this active refinement for each model, but each addition of new training data is still sampled randomly. In a separate study, we use self-energy uncertainty quantification to more efficiently select new training examples from unseen data. In particular, for the last three points of our training curves in Fig. 2 (1600, 1800, 2000 molecules), we employ active updates to the training data and compare the performance to random updates in Fig. 2. These results are presented in the SI, which show a slight improvement of MAEs in predcited band gap by $\sim$ 2 meV.

16

Data availability

All datasets used in this work will be made available in an open-source repository.

Code availability

The MBGF-Net code will be open-sourced upon publication of this work. Its implementation uses the fcDMFT code at https://github.com/ZhuGroup-Yale/fcdmft and PySCF at https://github.com/pyscf/pyscf.

Acknowledgements

Author Contributions

C.V. and T.Z. designed the project and wrote the manuscript. C.V. developed the graph neural network model and code. C.V., J.Li, and T.Z. developed the Green's function post-processing workflow. J.Li developed the BSE code. C.V., C.H., X.L.P., J.Liu performed Green's function calculations and data analyses. T.Z. supervised the project. All authors contribute to the discussion of the results as well as the writing and editing of the manuscript.

Additional information

The supplementary information is available for this paper.

References

(1) Kohn, W.; Sham, L. J. Self-Consistent Equations Including Exchange and Correlation Effects. *Phys. Rev.* **1965**, *140*, A1133–A1138.

(2) Cohen, A. J.; Mori-Sánchez, P.; Yang, W. Challenges for Density Functional Theory. *Chem. Rev.* **2012**, *112*, 289–320.

(3) Bartlett, R. J.; Musiał, M. Coupled-cluster theory in quantum chemistry. *Rev. Mod. Phys.* **2007**, *79*, 291–352.

(4) Hybertsen, M. S.; Louie, S. G. Electron Correlation in Semiconductors and Insulators: Band Gaps and Quasiparticle Energies. *Phys. Rev. B* **1986**, *34*, 5390–5413.

(5) Golze, D.; Dvorak, M.; Rinke, P. The GW compendium: A practical guide to theoretical photoemission spectroscopy. *Front. Chem.* **2019**, *7*, 377.

(6) Keith, J. A.; Vassilev-Galindo, V.; Cheng, B.; Chmiela, S.; Gastegger, M.; Müller, K.-R.; Tkatchenko, A. Combining Machine Learning and Computational Chemistry for Predictive Insights Into Chemical Systems. *Chem. Rev.* **2021**, *121*, 9816–9872.

(7) Westermayr, J.; Marquetand, P. Machine Learning for Electronically Excited States of Molecules. *Chem. Rev.* **2021**, *121*, 9873–9926.

(8) Deringer, V. L.; Bartók, A. P.; Bernstein, N.; Wilkins, D. M.; Ceriotti, M.; Csányi, G. Gaussian Process Regression for Materials and Molecules. *Chem. Rev.* **2021**, *121*, 10073–10141.

(9) Von Lilienfeld, O. A.; Müller, K. R.; Tkatchenko, A. Exploring chemical compound space with quantum-based machine learning. *Nat. Rev. Chem.* **2020**, *4*, 347–358.

(10) Behler, J.; Parrinello, M. Generalized neural-network representation of high-dimensional potential-energy surfaces. *Phys. Rev. Lett.* **2007**, *98*.

(11) Zhang, L.; Han, J.; Wang, H.; Car, R.; Weinan, E. Deep Potential Molecular Dynamics: A Scalable Model with the Accuracy of Quantum Mechanics. *Phys. Rev. Lett.* **2018**, *120*, 143001.

(12) Schütt, K. T.; Sauceda, H. E.; Kindermans, P. J.; Tkatchenko, A.; Müller, K. R. SchNet - A deep learning architecture for molecules and materials. *J. Chem. Phys.* **2018**, *148*, 241722.

(13) Smith, J. S.; Nebgen, B. T.; Zubatyuk, R.; Lubbers, N.; Devereux, C.; Barros, K.; Tretiak, S.; Isayev, O.; Roitberg, A. E. Approaching coupled cluster accuracy with a general-purpose neural network potential through transfer learning. *Nat. Commun.* **2019**, *10*, 1–8.

(14) Qiao, Z.; Welborn, M.; Anandkumar, A.; Manby, F. R.; Miller, T. F. OrbNet: Deep learning for quantum chemistry using symmetry-adapted atomic-orbital features. *J. Chem. Phys.* **2020**, *153*, 124111.

(15) Schütt, K. T.; Gastegger, M.; Tkatchenko, A.; Müller, K. R.; Maurer, R. J. Unifying machine learning and quantum chemistry with a deep neural network for molecular wavefunctions. *Nat. Commun.* **2019**, *10*, 1–10.

(16) Westermayr, J.; Maurer, R. J. Physically inspired deep learning of molecular excitations and photoemission spectra. *Chem. Sci.* **2021**, *12*, 10755–10764.

(17) Grisafi, A.; Fabrizio, A.; Meyer, B.; Wilkins, D. M.; Corminboeuf, C.; Ceriotti, M. Transferable Machine-Learning Model of the Electron Density. *ACS Cent. Sci.* **2019**, *5*, 57–64.

(18) Brockherde, F.; Vogt, L.; Li, L.; Tuckerman, M. E.; Burke, K.; Müller, K. R. Bypassing the Kohn-Sham equations with machine learning. *Nat. Commun.* **2017**, *8*, 1–10.

(19) Li, C.; Sharir, O.; Yuan, S.; Chan, G. K.-L. Image Super-resolution Inspired Electron Density Prediction. *arXiv:2402.12335* **2024**.

(20) Shao, X.; Paetow, L.; Tuckerman, M. E.; Pavanello, M. Machine learning electronic structure methods based on the one-electron reduced density matrix. *Nat. Commun.* **2023**, *14*, 1–9.

(21) Bai, Y.; Vogt-Maranto, L.; Tuckerman, M. E.; Glover, W. J. Machine learning the Hohenberg-Kohn map for molecular excited states. *Nat. Commun.* **2022**, *13*, 1–10.

(22) Hedin, L. New Method for Calculating the One-Particle Green's Function with Application to the Electron-Gas Problem. *Phys. Rev.* **1965**, *139*, A796–A823.

(23) Blase, X.; Duchemin, I.; Jacquemin, D.; Loos, P.-F. The Bethe–Salpeter Equation Formalism: From Physics to Chemistry. *J. Phys. Chem. Lett.* **2020**, *11*, 7371–7382.

(24) Zhu, T.; Chan, G. K. L. All-Electron Gaussian-Based G_0W_0 for Valence and Core Excitation Energies of Periodic Systems. *J. Chem. Theory Comput.* **2021**, *17*, 741.

(25) Lei, J.; Zhu, T. Gaussian-based quasiparticle self-consistent GW for periodic systems. *J. Chem. Phys.* **2022**, *157*, 214114.

(26) Nooijen, M.; Snijders, J. G. Coupled cluster Green's function method: Working equations and applications. *Int. J. Quantum Chem.* **1993**, *48*, 15–48.

(27) Peng, B.; Kowalski, K. Green's Function Coupled-Cluster Approach: Simulating Photoelectron Spectra for Realistic Molecular Systems. *J. Chem. Theory Comput.* **2018**, *14*, 4335–4352.

(28) Zhu, T.; Jiménez-Hoyos, C. A.; McClain, J.; Berkelbach, T. C.; Chan, G. K.-L. Coupled-cluster impurity solvers for dynamical mean-field theory. *Phys. Rev. B* **2019**, *100*, 115154.

(29) Laughon, K.; Yu, J. M.; Zhu, T. Periodic Coupled-Cluster Green's Function for Photoemission Spectra of Realistic Solids. *J. Phys. Chem. Lett.* **2022**, *13*, 9122–9128.

(30) Phillips, J. J.; Zgid, D. Communication: The description of strong correlation within self-consistent Green's function second-order perturbation theory. *J. Chem. Phys.* **2014**, *140*, 241101.

(31) Hirata, S.; Hermes, M. R.; Simons, J.; Ortiz, J. V. General-Order Many-Body Green's Function Method. *J. Chem. Theory Comput.* **2015**, *11*, 1595–1606.

(32) Banerjee, S.; Sokolov, A. Y. Algebraic Diagrammatic Construction Theory for Simulating Charged Excited States and Photoelectron Spectra. *J. Chem. Theory Comput.* **2023**, *19*, 3053.

(33) Ronca, E.; Li, Z.; Jimenez-Hoyos, C. A.; Chan, G. K. L. Time-Step Targeting Time-Dependent and Dynamical Density Matrix Renormalization Group Algorithms with ab Initio Hamiltonians. *J. Chem. Theory Comput.* **2017**, *13*, 5560–5571.

(34) Gull, E.; Millis, A. J.; Lichtenstein, A. I.; Rubtsov, A. N.; Troyer, M.; Werner, P. Continuous-time Monte Carlo methods for quantum impurity models. *Rev. Mod. Phys.* **2011**, *83*, 349–404.

(35) Kotliar, G.; Savrasov, S. Y.; Haule, K.; Oudovenko, V. S.; Parcollet, O.; Marianetti, C. A. Electronic structure calculations with dynamical mean-field theory. *Rev. Mod. Phys.* **2006**, *78*, 865–951.

(36) Zhu, T.; Cui, Z.-H.; Chan, G. K.-L. Efficient formulation of ab initio quantum embedding in periodic systems: Dynamical mean-field theory. *J. Chem. Theory Comput.* **2020**, *16*, 141–153.

(37) Zhu, T.; Chan, G. K.-L. Ab Initio Full Cell GW+DMFT for Correlated Materials. *Phys. Rev. X* **2021**, *11*, 021006.

(38) Lan, T. N.; Kananenka, A. A.; Zgid, D. Communication: Towards ab initio self-energy embedding theory in quantum chemistry. *J. Chem. Phys.* **2015**, *143*, 241102.

(39) Venturella, C.; Hillenbrand, C.; Li, J.; Zhu, T. Machine Learning Many-Body Green's Functions for Molecular Excitation Spectra. *J. Chem. Theory Comput.* **2024**, *20*, 143–154.

(40) Arsenault, L. F.; Lopez-Bezanilla, A.; Von Lilienfeld, O. A.; Millis, A. J. Machine learning for many-body physics: The case of the Anderson impurity model. *Phys. Rev. B* **2014**, *90*, 155136.

(41) Dong, X.; Gull, E.; Wang, L. Equivariant neural network for Green's functions of molecules and materials. *Phys. Rev. B* **2024**, *109*, 075112.

(42) Batzner, S.; Musaelian, A.; Sun, L.; Geiger, M.; Mailoa, J. P.; Kornbluth, M.; Molinari, N.; Smidt, T. E.; Kozinsky, B. E(3)-equivariant graph neural networks for data-efficient and accurate interatomic potentials. *Nat. Commun.* **2022**, *13*, 2453.

(43) Reiser, P.; Neubert, M.; Eberhard, A.; Torresi, L.; Zhou, C.; Shao, C.; Metni, H.; van Hoesel, C.; Schopmans, H.; Sommer, T.; Friederich, P. Graph neural networks for materials science and chemistry. *Commun. Mater.* **2022**, *3*, 93.

(44) Knizia, G. Intrinsic atomic orbitals: An unbiased bridge between quantum theory and chemical concepts. *J. Chem. Theory Comput.* **2013**, *9*, 4834–4843.

(45) Qiao, Z.; Christensen, A. S.; Welborn, M.; Manby, F. R.; Anandkumar, A.; Miller, T. F. Informing geometric deep learning with electronic interactions to accelerate quantum chemistry. *Proc. Natl. Acad. Sci. U. S. A.* **2022**, *119*, e2205221119.

(46) Wilhelm, J.; Seewald, P.; Golze, D. Low-Scaling GW with Benchmark Accuracy and Application to Phosphorene Nanosheets. *J. Chem. Theory Comput.* **2021**, *17*, 1662–1677.

(47) Rupp, M.; Tkatchenko, A.; Müller, K. R.; Von Lilienfeld, O. A. Fast and accurate modeling of molecular atomization energies with machine learning. *Phys. Rev. Lett.* **2012**, *108*, 058301.

(48) Ramakrishnan, R.; Dral, P. O.; Rupp, M.; Von Lilienfeld, O. A. Quantum chemistry structures and properties of 134 kilo molecules. *Sci. Data* **2014**, *1*, 1–7.

(49) Dunning, T. H. Gaussian basis sets for use in correlated molecular calculations. I. The atoms boron through neon and hydrogen. *J. Chem. Phys.* **1989**, *90*, 1007–1023.

(50) Woon, D. E.; Dunning, T. H. Gaussian basis sets for use in correlated molecular calculations. III. The atoms aluminum through argon. *J. Chem. Phys.* **1993**, *98*, 1358–1371.

(51) Sun, Q.; Zhang, X.; Banerjee, S.; Bao, P.; Barbry, M.; Blunt, N. S.; Bogdanov, N. A.; Booth, G. H.; Chen, J.; Cui, Z. H.; Eriksen, J. J.; Gao, Y.; Guo, S.; Hermann, J.; Hermes, M. R.; Koh, K.; Koval, P.; Lehtola, S.; Li, Z.; Liu, J.; Mardirossian, N.; McClain, J. D.; Motta, M.; Mussard, B.; Pham, H. Q.; Pulkin, A.; Purwanto, W.; Robinson, P. J.; Ronca, E.; Sayfutyarova, E. R.; Scheurer, M.; Schurkus, H. F.; Smith, J. E.; Sun, C.; Sun, S. N.; Upadhyay, S.; Wagner, L. K.; Wang, X.; White, A.; Whitfield, J. D.; Williamson, M. J.; Wouters, S.; Yang, J.; Yu, J. M.; Zhu, T.; Berkelbach, T. C.; Sharma, S.; Sokolov, A. Y.; Chan, G. K. L. Recent developments in the PySCF program package. *J. Chem. Phys.* **2020**, *153*, 024109.

(52) Adamo, C.; Barone, V. Toward reliable density functional methods without adjustable parameters: The PBE0 model. *J. Chem. Phys.* **1999**, *110*, 6158–6170.

(53) Fediai, A.; Reiser, P.; Peña, J. E. O.; Wenzel, W.; Friederich, P. Interpretable delta-learning of GW quasiparticle energies from GGA-DFT. *Mach. Learn. Sci. Technol.* **2023**, *4*, 035045.

(54) Wolkin, M. V.; Jorne, J.; Fauchet, P. M.; Allan, G.; Delerue, C. Electronic States and Luminescence in Porous Silicon Quantum Dots: The Role of Oxygen. *Phys. Rev. Lett.* **1999**, *82*, 197–200.

(55) Zauchner, M. G.; Horsfield, A.; Lischner, J. Accelerating GW calculations through machine-learned dielectric matrices. *npj Comput. Mater.* **2023**, *9*, 184.

(56) Gao, W.; Tang, Z.; Zhao, J.; Chelikowsky, J. R. Efficient Full-Frequency GW Calculations Using a Lanczos Method. *Phys. Rev. Lett.* **2024**, *132*, 126402.

(57) Kühne, T. D.; Iannuzzi, M.; Del Ben, M.; Rybkin, V. V.; Seewald, P.; Stein, F.; Laino, T.; Khaliullin, R. Z.; Schütt, O.; Schiffmann, F.; Golze, D.; Wilhelm, J.; Chulkov, S.; Bani-Hashemian, M. H.; Weber, V.; Borštnik, U.; Taillefumier, M.; Jakobovits, A. S.; Lazzaro, A.; Pabst, H.; Müller, T.; Schade, R.; Guidon, M.; Andermatt, S.; Holmberg, N.; Schenter, G. K.; Hehn, A.; Bussy, A.; Belleflamme, F.; Tabacchi, G.; Glöß, A.; Lass, M.; Bethune, I.; Mundy, C. J.; Plessl, C.; Watkins, M.; VandeVondele, J.; Krack, M.; Hutter, J. CP2K: An electronic structure and molecular dynamics software package - Quickstep: Efficient and accurate electronic structure calculations. *J. Chem. Phys.* **2020**, *152*, 194103.

(58) Zhu, T.; Peng, L.; Zhai, H.; Cui, Z.-H.; Chan, G. K.-L. Towards an exact electronic quantum many-body treatment of Kondo correlation in magnetic impurities. *arXiv:2405.18709* **2024**.

(59) Taube, A. G.; Bartlett, R. J. Frozen natural orbital coupled-cluster theory: Forces and application to decomposition of nitroethane. *J. Chem. Phys.* **2008**, *128*, 164101.

(60) Li, J.; Zhu, T. Interacting-bath dynamical embedding for capturing non-local electron correlation in solids. *arXiv:2406.07531* **2024**.

(61) Fey, M.; Lenssen, J. E. In *ICLR 2019 Workshop on Representation Learning on Graphs and Manifolds*, New Orleans, USA, 2019.

(62) Paszke, A.; Gross, S.; Chintala, S.; Chanan, G.; Yang, E.; DeVito, Z.; Lin, Z.; Desmaison, A.; Antiga, L.; Lerer, A. Automatic differentiation in PyTorch. *NIPS-W* **2017**.

(63) Veličković, P.; Cucurull, G.; Casanova, A.; Romero, A.; Liò, P.; Bengio, Y. In *International Conference on Learning Representations*, 2018.

(64) Li, Y.; Gu, C.; Dullien, T.; Vinyals, O.; Kohli, P. In *International conference on machine learning*, 2019.